Available online at www.sciencedirect.com
SCIENCE DIRECT®
International Journal of Heat and Mass Transfer 48 (2005) 1225–1235
International Journal of HEAT and MASS TRANSFER
www.elsevier.com/locate/ijhmt

Embedded converging surface microchannels for minimized friction and thermal irreversibilities

G.F. Naterer *

Department of Mechanical and Manufacturing Engineering, University of Manitoba, 15 Gillson Street, Winnipeg, Manitoba, Canada R3T 2N2

Received 12 March 2004; received in revised form 18 October 2004
Available online 15 December 2004

Abstract

Embedded converging surface microchannels are developed as effective new ways of reducing entropy production in boundary layer flow with convective heat transfer. A similarity solution with slip-flow boundary conditions is developed to find the spatial distributions of velocity, temperature, wall shear stress and wall heat flux. Mixed Knudsen number conditions along the surface require both slip-flow and no-slip formulations to be combined in an integral solution. Predicted results from the method of EBSM (entropy based surface micro-profiling) are presented for the optimized microchannel aspect ratio, spacing between adjacent microchannels and the angles characterizing the converging microchannels.

1. Introduction

Microfluidics technology has promising potential in numerous practical applications, i.e., bio-chemical sensors, microelectronics cooling, turbomachinery for micro heat engines and others. Gad-el-Hak [1] presents a comprehensive review of recent advances in microfluidics technology. This article considers embedded surface microdevices and microchannels for purposes of thermal control and reduced entropy production. For example, pulsating micropistons or microtabs enabled by micro-engines beneath a heated surface could be used to delay boundary layer separation and reduce wall friction. In this article, surface manipulations with open microchannels are considered, so that exergy losses in external flow can be minimized. System input power can be reduced with this new method, in view of drag reduction and heat transfer enhancement, when local rates of entropy production are minimized.

Past research [2] has shown that certain converging and diverging microchannel profiles can affect the boundary layer separation downstream of a curved surface. Such flow control can be used for practical purposes. For example, a shear-driven surface film can be ejected by the surrounding air stream to reduce icing of aircraft engines [2]. Adaptive surface micromachining involves a new type of controlled surface roughness, with an added benefit of allowing more detailed design of surface geometrical parameters. This article focuses on passive (non-moving) surface manipulations. But it is anticipated that future developments could extend these techniques to moving surface components optimized at micron and sub-micron scales.

Liquid flows in microchannels can be generated by a pressure difference, electrical potential difference or

* Tel.: +1 204 474 9804; fax: +1 204 275 7507.
E-mail address: natererg@cc.umanitoba.ca

0017-9310/$ - see front matter © 2004 Elsevier Ltd. All rights reserved.
doi:10.1016/j.ijheatmasstransfer.2004.10.016

Nomenclature

d	depth of microchannel (m)
k	thermal conductivity (W/m K)
K_1	slip coefficient
Kn	Knudsen number (mean free path divided by characteristic length scale)
L	length of plate (m)
n	number of microchannels
q'	heat flow per unit length (W/m)
Re	Reynolds number
T	temperature (K)
u	freestream velocity
W	width of plate (m)
W_s	width of microchannel (m)

Greek symbols

ϕ	irreversibility distribution ratio
λ	surface parameter, $(W_s + 2d)/W$
μ	dynamic viscosity (kg/m s)
ζ	surface parameter, d/W

Subscripts

w	wall
∞	ambient (freestream) value

thermocapillary pumping. Depending on the local Knudsen number, slip-flow conditions may be experienced [3]. Pressure-driven flow of water through trapezoidal microchannels was investigated by Qu et al. [4]. Various cross-sectional profiles of microchannels have been studied previously, including circular profiles of microtubes [5], rectangular microchannels exposed to a freestream [2] and others. Microfluidic transport is largely affected by interfacial phenomena, such as surface tension and roughness effects. Thermocapillary pumping is a surface tension based mechanism of microfluidic pumping action. Important parameters affecting such pumping action include thermal conductivity and velocity of the liquid droplets [6]. Due to surface tension variations with temperature, differences of tension forces between both ends of a droplet lead to an effective pressure difference across the droplet, thereby inducing microfluidic motion.

By following the trajectory of a microscopic latex bead through water, Wang et al. [7] claimed that temporary conversions between internal and mechanical energy within the water molecules lead to microfluidic violation of the Second Law of Thermodynamics. The 6-μm diameter bead was pulled through water by an infrared laser confining the bead between two beams. But occasionally the bead was pushed ahead when enough water molecules bounced into the bead simultaneously with a more orderly arrangement of molecules (analogous to a barge suddenly jumping ahead of a tugboat pulling it). Despite the follow-up skepticism and controversy surrounding such claims [8], the Second Law considerations of microfluidic transport remain a relatively new and undocumented subject, particularly in the engineering literature.

However, past research has outlined the significance of the Second Law in thermal engineering applications. The principle of equipartition of forces (EoF) and a lower bound on entropy production are used by Nummedal and Kjelstrup [9] to identify certain operating boundary conditions for better heat exchanger performance. Naterer and Camberos [10] presented a review of past numerical studies in such applications, including heat exchangers, power generation, aircraft sub-systems and materials processing. Johannessen et al. [11] reported that the total irreversibilities within a heat exchanger are minimized when local entropy production is constant throughout all parts of the system.

Furthermore, an apparent entropy production difference, which arises from an unexpected difference between positive definite and transport forms of the Second Law, offers a useful error indicator for thermofluid applications [12]. Turbulent entropy production in a plane jet with quasi-periodic lateral oscillations is documented by Cervantez and Solorio [13]. Modeling of entropy transport processes in other flow regimes, such as phase change heat transfer [14–16], convective heat transfer [17], compressible flows [18,19] and others [20] has been reported in the technical literature.

When performing optimization studies, such as minimized entropy production in thermofluid systems, surface shape is often used as a key design parameter. Search methods for thermal and fluid system optimization have been outlined by Jaluria [21]. Geometric shape optimization of aircraft surfaces can be successfully accomplished by genetic algorithms [22] and adaptive response surface methods [23]. For certain geometrical configurations, methods of optimization based on multi-variable calculus and Lagrange multipliers [21] can be utilized successfully.

This paper applies analytical methods to the optimization of external flow configurations, which exhibit reduced entropy production due to slip-flow conditions within embedded microchannels along the surface. Unlike past methods which have optimized macroscale characteristics of surface geometries, this paper offers new insight regarding how surface micro-profiling can

reduce entropy production of external flows past standard configurations and surfaces.

2. Fluid flow and heat transfer formulation

External flow past a flat surface with embedded open microchannels is considered (see Figs. 1 and 2). This flow configuration closely resembles flat plate boundary layer flow, with a Blasius similarity solution for streamwise changes of flow variables (documented in Ref. [16]). The open microchannels are aligned parallel to the incoming flow along the surface, with micron or sub-micron scale depth. Unlike random surface roughness, the well-controlled geometrical profiles of these embedded microchannels allow effective optimization for drag reduction and heat transfer enhancement. This newly proposed technique is called EBSM (entropy based surface micro-profiling). A basic geometry of flat plate flow is considered in this article, but once the performance and feasibility are well established, it is viewed that the technique can be readily extended to more complex geometries.

In the x–z-direction (i.e., side view within a microchannel), a Couette-type flow is encountered. A Couette flow refers to a 1-D shear layer enclosed by fixed velocities at both edges of the layer. For example, a linear variation of velocity occurs between a moving plate and a stationary wall below the plate. In the case of the open microchannel, a non-zero Blasius velocity and slip velocity are encountered at the top and base of the microchannel. Diffusion dominated transport of momentum in the z-direction is considered to yield a similar linear profile between both edge velocities. The slope of this profile decreases in the x-direction, as the top velocity changes in the slip-flow pattern of the boundary layer development.

A front-view of the plate in the z–y-direction at a fixed x-location reveals other aspects of the varying velocity profile. An analogous assumption to the no-slip Blasius solution is adopted, whereby cross-stream flow is neglected and the z- and y-velocities are assumed to be negligible, relative to the streamwise (x-direction) velocity component. A "driven cavity flow" refers to 2-D shear-driven flow within an open cavity. This type of driven cavity flow does not represent the current flow configuration, since the fluid at the top of the cavity is flowing perpendicular to the cross-section of the cavity, rather than parallel to the cross-section.

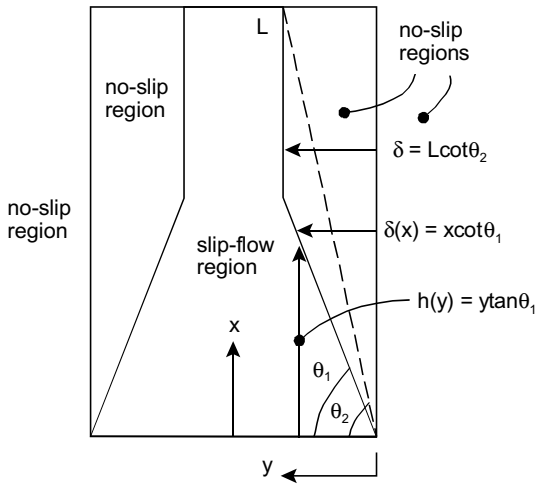

Fig. 2. Geometric configuration of converging microchannels.

Transition between slip-flow and no-slip regimes occurs at the top corners of the embedded microchannels. Consider a slip-flow embedded microchannel, with a Knudsen number and characteristic length based on both depth and width. At the top corners, the near-wall slip-flow profile approaches no-slip behavior before reaching the top edge of the microchannel. This transition occurs because the local Knudsen number decreases at the top edges of the microchannel. This region of transition may produce a small sub-micron semi-circular type zone of influence at the top corners.

Unfortunately, little or no experimental data (to the author's knowledge) has been reported in the technical literature regarding such slip-flow variations arising from this transition. Past studies have mainly reported slip-flow coefficients based on measured mass flow rate slopes against various pressure differences in *closed*

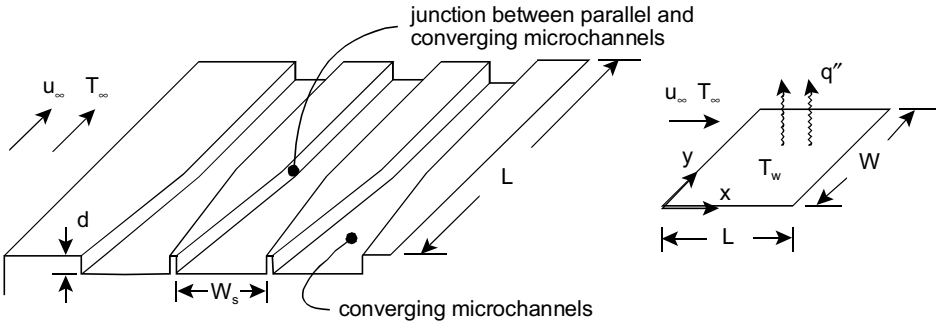

Fig. 1. Schematic of embedded surface microchannels in external flow.

microchannels. The current transition regime and mixed Knudsen numbers would not arise in those cases. Furthermore, the measurements yield a single (net) coefficient, without spatial variations across the microchannel. In this study, a single coefficient simulates a spatial variation and transition regime in a similar fashion.

Analytical solutions of laminar boundary layer flow can be determined by methods of similarity variable analysis (documented in Ref. [16]). The predicted velocity field, u, from this method for flat plate boundary layer flow can be expressed in terms of a similarity variable, η, freestream velocity, u_∞, and a stream function derivative as follows,

$$\frac{u}{u_\infty} = f'(\eta) \tag{1}$$

where

$$\eta = y\sqrt{\frac{u_\infty}{vx}} \tag{2}$$

Transforming the 2-D, steady, laminar boundary layer equations with this similarity variable, the governing equation for mass and momentum transport within the boundary layer becomes

$$f'''(\eta) + \frac{1}{2}f(\eta)f''(\eta) = 0 \tag{3}$$

This non-linear ordinary differential equation is solved by a Runge-Kutta method, subject to boundary conditions of $f'(\infty) = 1$ and $f(0) = 0$. The no-slip condition at the wall is $f'(0) = 0$.

An analytical solution can be obtained from successive integrations as follows,

$$u^* = \frac{u}{u_\infty} = f'(\eta) = \frac{\int_0^\eta \left[\exp\left(-\int_0^\eta f/2\,\mathrm{d}\eta\right)\right]\mathrm{d}\eta}{\int_0^\infty \left[\exp\left(-\int_0^\eta f/2\,\mathrm{d}\eta\right)\right]\mathrm{d}\eta} \tag{4}$$

It can be shown that the functional forms of the momentum and thermal energy equations are equivalent, so a similar procedure yields the following approximation for the non-dimensional temperature within the boundary layer,

$$\theta(\eta) = \frac{T - T_w}{T_\infty - T_w} = \frac{\int_0^\eta \left[\exp\left(-Pr\int_0^\eta f/2\,\mathrm{d}\eta\right)\right]\mathrm{d}\eta}{\int_0^\infty \left[\exp\left(-Pr\int_0^\eta f/2\,\mathrm{d}\eta\right)\right]\mathrm{d}\eta} \tag{5}$$

When the Prandtl number of the fluid is close to 1 (common fluids such as air), the previous expressions for non-dimensional velocity and temperature become identical.

For the case of a slip-flow condition at the wall, the boundary condition involves the non-zero wall velocity and the spatial gradient of velocity (second derivative of the stream function at the wall), so that

$$f'(0) = K_1 f''(0) \tag{6}$$

where

$$K_1 = \left(\frac{2-\sigma}{\sigma}\right) Kn_x Re_x^{1/2} \tag{7}$$

Also, Kn_x and Re_x are the local Knudsen and Reynolds numbers, respectively. This boundary condition implies that the slip-flow velocity at the wall increases with higher velocity gradients at the wall.

After the third-order differential equation is solved, subject to the slip-flow boundary condition, the resulting stream function, $f(\eta)$, can be numerically differentiated to yield the velocity field and wall shear stress, τ_w, distributions, i.e.,

$$\tau_w = \frac{\rho^{1/2}\mu^{1/2}u_\infty^{3/2}}{x^{1/2}} f''(0) \tag{8}$$

Re-arranging this result in terms of the local Reynolds number and deriving an analogous result for the Nusselt number (note: analogous results for both specified wall temperature and heat flux cases), yields [16]

$$\frac{\tau_w}{\rho u_\infty^2} = f''(0)\cdot Re_x^{-1/2} \tag{9}$$

$$Nu_x = \frac{hx}{k} = \theta'(0)\cdot Re_x^{1/2} \tag{10}$$

Within the embedded microchannels, the wall shear stress is characterized by slip-flow momentum exchange and intermolecular interactions near the microchannel walls. Unlike macroscale systems with a no-slip condition at the wall, the slip-flow conditions and spatial changes in the microwetting ability of the fluid can lead to lower shear stresses along the walls. Such variations have been previously investigated for gases [3] and liquids [24]. Choi et al. [24] have reported higher water flow rates induced by a different surface coating along a microchannel wall, thereby indicating a variation of slip velocity and shear stress along the wall. Such slip-flow effects increased when the channel height decreased and the wall shear stress increased.

The percent reduction of wall shear stress due to the slip-flow condition, as compared to the no-slip solution, can be determined from the previous similarity solution. The result can be expressed as $100\%(0.3321 - f''(0))$, where $f''(0)$ refers to the result from the slip-flow solution. The value of 0.3321 corresponds to the conventional Blasius solution with a no-slip velocity at the wall [19]. Martin and Boyd [3] investigate the validity of key assumptions adopted in this similarity solution analysis. At all locations except the leading edge, it is considered that the streamwise velocity gradient is much smaller than the cross-stream (y-direction) gradient. Combining both Blasius and Stokes flow solutions allows the numerical predictions to accommodate the singularity at $x = 0$ [3].

3. Predicted friction and thermal irreversibilities

In this section, entropy production related to converging embedded microchannels is considered (see

Fig. 2). Friction and thermal irreversibilities are included within the total entropy production. The convective heat transfer involves laminar external flow past the flat plate in steady-state conditions. Local fluid acceleration due to an area change within a converging microchannel interacts with the boundary layer above the microchannel. As a result, a closed microchannel mass balance cannot be directly applied to near-wall variations of fluid velocity.

The total entropy production over a plate of length L and a width of W consists of a thermal irreversibility and a friction irreversibility, which can be expressed as [16]

$$\dot{S}_{\text{gen}} = \left(\frac{q''}{T_\infty}\right)^2 \int_0^W \int_0^L \frac{\mathrm{d}x\,\mathrm{d}y}{h} + \frac{u_\infty}{T_\infty} \int_0^W \int_0^L \tau_{\text{w}}\,\mathrm{d}x\,\mathrm{d}y \tag{11}$$

Substituting the previous correlations for the convection coefficient, h (based on the Nusselt number), and wall shear stress, τ_{w}, the total entropy production becomes

$$\dot{S}_{\text{gen}} = \left(\frac{q''^2 v^2}{kT_\infty^2 u_\infty^2}\right) \int_0^{Re_L} \int_0^W \frac{Re_x^{1/2}}{\theta'(0)}\mathrm{d}y\,\mathrm{d}Re_x + \left(\frac{u_\infty \mu}{T_\infty}\right) \int_0^{Re_L} \int_0^W f''(0) Re_x^{-1/2}\mathrm{d}y\,\mathrm{d}Re_x \tag{12}$$

The integral from $0 \leqslant y \leqslant W$ consists of n integrations over each microchannel surface and the remaining no-slip portion of the plate, which is interspersed between these microchannels. The plate can be sub-divided into slip-flow regions (n microchannels; integrated over $0 \leqslant y \leqslant W_{\text{s}} + 2d$) and the remaining no-slip regions (integrated over $0 \leqslant y \leqslant W - nW_{\text{s}}$). The flat plate region of slip-flow conditions is further sub-divided over the parallel microchannel section and the converging section (integrated over $0 \leqslant y \leqslant \delta$; see Fig. 2).

The no-slip region is also sub-divided into two distinct parts. When both parts are grouped together, the sub-divided regions entail a slip-flow integral (n microchannels; integrated over $0 \leqslant y \leqslant W_{\text{s}} + 2d$) and a no-slip integral (integrated over $0 \leqslant y \leqslant W - nW_{\text{s}}$) minus an integral involving slip minus no-slip integrands ($2n$ sections; integrated over $0 \leqslant y \leqslant \delta$). Then, the total entropy production over the plate becomes

$$\begin{aligned}\dot{S}_{\text{gen}} = {} & \left(\frac{q''^2 v^2}{kT_\infty^2 u_\infty^2}\right)\left\{ n \int_0^{Re_L} \int_0^{W_{\text{s}}+2d} \frac{Re_x^{1/2}}{\theta'_{\text{s}}(0)}\mathrm{d}y\,\mathrm{d}Re_x + \int_0^{Re_L} \int_0^{W-nW_{\text{s}}} \frac{Re_x^{1/2}}{\theta'_{\text{ns}}(0)}\mathrm{d}y\,\mathrm{d}Re_x \right\} \\ & + \left(\frac{u_\infty^2 \mu}{T_\infty}\right)\left\{ n \int_0^{Re_L} \int_0^{W_{\text{s}}+2d} \frac{f''_{\text{s}}(0)}{Re_x^{1/2}}\mathrm{d}y\,\mathrm{d}Re_x + \int_0^{Re_L} \int_0^{W-nW_{\text{s}}} \frac{f''_{\text{s}}(0)}{Re_x^{1/2}}\mathrm{d}y\,\mathrm{d}Re_x \right\} + \dot{S}_{\text{gen,f}} + \dot{S}_{\text{gen,h}}\end{aligned} \tag{13}$$

The subscripts s and ns refer to slip-flow and no-slip regions, respectively. Also, the latter two integrals, $\dot{S}_{\text{gen,f}}$ and $\dot{S}_{\text{gen,h}}$, refer to the wall friction irreversibility difference and wall thermal irreversibility difference due to slip minus no-slip conditions, respectively, i.e.,

$$\dot{S}_{\text{gen,h}} = -\left(\frac{q''^2 v^2}{kT_\infty^2 u_\infty^2}\right) 2n \int_0^{Re_L} \int_0^{\delta} \left(\frac{Re_x^{1/2}}{\theta'_{\text{s}}(0)} - \frac{Re_x^{1/2}}{\theta'_{\text{ns}}(0)}\right)\mathrm{d}y\,\mathrm{d}Re_x \tag{14}$$

$$\dot{S}_{\text{gen,f}} = -\left(\frac{u_\infty^2 \mu}{T_\infty}\right) 2n \int_0^{Re_L} \int_0^{\delta} \left(\frac{f''_{\text{s}}(0)}{Re_x^{1/2}} - \frac{f''_{\text{ns}}(0)}{Re_x^{1/2}}\right)\mathrm{d}y\,\mathrm{d}Re_x \tag{15}$$

Then, the total entropy production over the plate can be expressed as a sum of entropy production rates for parallel microchannels (subscript p) and irreversibility difference integrals for converging microchannels ($\dot{S}_{\text{gen,f}}$ plus $\dot{S}_{\text{gen,h}}$), i.e.,

$$\dot{S}_{\text{gen}} = \dot{S}_{\text{gen,p}} + \dot{S}_{\text{gen,h}} + \dot{S}_{\text{gen,f}} \tag{16}$$

The irreversibility difference integrals depend on the base and outlet expansion angles, θ_1 and θ_2. For the case of thermal irreversibilities,

$$\dot{S}_{\text{gen,h}} = -\left(\frac{q''^2 v^{1/2}}{kT_\infty^2 u_\infty^{1/2}}\right) 2n \left(\frac{1}{\theta'_{\text{s}}(0)} - \frac{1}{\theta'_{\text{ns}}(0)}\right) \times \int_0^{L\cot\theta_2} \int_h^L x^{1/2}\mathrm{d}x\,\mathrm{d}y \tag{17}$$

which can be integrated to yield

$$\dot{S}_{\text{gen,h}} = -\left(\frac{q''^2 v^{1/2}}{kT_\infty^2 u_\infty^{1/2}}\right) \frac{4}{3} n \left(\frac{1}{\theta'_{\text{s}}(0)} - \frac{1}{\theta'_{\text{ns}}(0)}\right) L^{5/2} \times \left(\cot\theta_2 - \frac{2}{5}\cot^{5/2}\theta_2 \tan^{3/2}\theta_1\right) \tag{18}$$

Re-arranging and simplifying,

$$\dot{S}_{\text{gen,h}} = -\left(\frac{q'^2 v}{kT_\infty^2 u_\infty}\right) 0.921 n K_1^{1.11} \times \left(\cot\theta_2 - \frac{2}{5}\cot^{5/2}\theta_2 \tan^{3/2}\theta_1\right) Re_L^{1/2} \tag{19}$$

Similarly, the friction irreversibility difference integral can be evaluated as follows,

$$\dot{S}_{\text{gen,f}} = -\left(\frac{u_\infty^{5/2} \rho^{1/2} \mu^{1/2}}{T_\infty}\right) 2n \left(f''_{\text{s}}(0) - f''_{\text{ns}}(0)\right) \times \int_0^{L\cot\theta_2} \int_h^L x^{-1/2}\mathrm{d}x\,\mathrm{d}y \tag{20}$$

which is integrated to give

$$\dot{S}_{\text{gen,f}} = -\left(\frac{u_\infty^{5/2} \rho^{1/2} \mu^{1/2}}{T_\infty}\right) 4n \left(f''_{\text{s}}(0) - f''_{\text{ns}}(0)\right) L^{3/2} \times \left(\cot\theta_2 - \frac{2}{3}\cot^{3/2}\theta_2 \tan^{1/2}\theta_1\right) \tag{21}$$

Then, re-arranging and simplifying leads to

$$\dot{S}_{\mathrm{gen,f}} = -\left(\frac{u_\infty^2\mu^2}{\rho T_\infty}\right)\left(\frac{5.56}{4.185+0.96K_1^{1.11}}-1.328\right)n \times\left(\cot\theta_2-\frac{2}{3}\cot^{3/2}\theta_2\tan^{1/2}\theta_1\right)Re_L^{3/2} \tag{22}$$

After combining the integrals together and expressing the results in terms of non-dimensional variables, the total entropy production per unit width of plate becomes

$$\begin{aligned}\frac{\dot{S}_{\mathrm{gen}}}{W} &= \left(\frac{q'^2}{kT_\infty^2}\right)\left[(0.461K_1^{1.11}n\lambda+2.008(1+2n\varsigma))Re_L^{-1/2}\right.\\ &\quad\left.-\frac{0.921}{Re_W}nK_1^{1.11}\left(\cot\theta_2-\frac{2}{5}\cot^{5/2}\theta_2\tan^{3/2}\theta_1\right)Re_L^{1/2}\right]\\ &\quad-\left(\frac{u_\infty^2\mu}{T_\infty}\right)\left[\left(\frac{5.56}{4.185+0.96K_1^{1.11}}-1.328\right)\frac{n}{Re_W}\right.\\ &\quad\left.\times\left(\cot\theta_2-\frac{2}{3}\cot^{3/2}\theta_2\tan^{1/2}\theta_1\right)\right]Re_L^{3/2}\\ &\quad+\left(\frac{u_\infty^2\mu}{T_\infty}\right)\left[\frac{2.78n\lambda}{4.185+0.96K_1^{1.11}}\right.\\ &\quad\left.+0.664(1+2n\varsigma-n\lambda)\right]Re_L^{1/2}\end{aligned} \tag{23}$$

where $\lambda = (W_s + 2d)/W$ and $\varsigma = d/W$. By specifying the appropriate base and exit expansion angles in this result, other special cases may be obtained (such as parallel microchannels or plate without microchannels).

The optimal Reynolds number will minimize the entropy production rate. It is determined by differentiating the previous expression with respect to Re_L and setting that result equal to zero, thereby yielding

$$Re_{L,\mathrm{opt}} = \frac{-c_2-c_3+\sqrt{(c_2+c_3)^2+12c_1\cdot c_4}}{6c_4} \tag{24}$$

where

$$c_1 = \left(\frac{q'^2}{kT_\infty^2}\right)(0.461K_1^{1.11}n\lambda+2.008(1+2n\varsigma)) \tag{25}$$

$$c_2 = -\left(\frac{q'^2}{kT_\infty^2}\right)\frac{0.921}{Re_W}nK_1^{1.11}\left(\cot\theta_2-\frac{2}{5}\cot^{5/2}\theta_2\tan^{3/2}\theta_1\right) \tag{26}$$

$$c_3 = \left(\frac{u_\infty^2\mu}{T_\infty}\right)\left(\frac{2.78n\lambda}{4.185+0.96K_1^{1.11}}+0.664(1+2n\varsigma-n\lambda)\right) \tag{27}$$

$$c_4 = -\left(\frac{u_\infty^2\mu}{T_\infty}\right)\left(\frac{5.56}{4.185+0.96K_1^{1.11}}-1.328\right)\frac{n}{Re_W} \times\left(\cot\theta_2-\frac{2}{3}\cot^{3/2}\theta_2\tan^{1/2}\theta_1\right) \tag{28}$$

Multiplying this optimal Reynolds number by kinematic viscosity and dividing by the freestream velocity yields the optimal plate length. At this particular plate length, the rate of total entropy production is minimized.

Furthermore, the entropy generation number, N_s, is evaluated as follows,

$$N_s = \frac{\dot{S}_{\mathrm{gen}}}{\dot{S}_{\mathrm{gen,opt}}} = \alpha\left(\frac{Re_L}{Re_{L,\mathrm{opt}}}\right)^{-1/2}+\beta\left(\frac{Re_L}{Re_{L,\mathrm{opt}}}\right)^{1/2}+\gamma\left(\frac{Re_L}{Re_{L,\mathrm{opt}}}\right)^{3/2} \tag{29}$$

where the leading coefficients are determined from

$$\alpha = \frac{c_1}{c_1+(c_2+c_3)Re_{L,\mathrm{opt}}+c_4Re_{L,\mathrm{opt}}^2} \tag{30}$$

$$\beta = \frac{c_2+c_3}{c_1/Re_{L,\mathrm{opt}}+(c_2+c_3)+c_4Re_{L,\mathrm{opt}}} \tag{31}$$

$$\gamma = \frac{c_4}{c_1/Re_{L,\mathrm{opt}}^2+(c_2+c_3)/Re_{L,\mathrm{opt}}+c_4} \tag{32}$$

The previous result for the optimal Reynolds number ($Re_{L,\mathrm{opt}}$ written in terms of c_1, c_2, c_3 and c_4) is substituted into these expressions, thereby yielding a closed form expression for the entropy generation number.

For a fixed rate of heat transfer, q', a large surface length would reduce the temperature difference (between fluid and wall) required to achieve q', thereby reducing the input power needed to maintain T_w. But the surface friction increases with a larger surface length, thereby increasing the input power to establish a certain flow rate of fluid passing over the surface. A smaller surface length reduces the total friction and input power, but at the expense of a higher thermal irreversibility and input power associated with the higher temperature difference to maintain q'.

The best compromise from an overall energy utilization viewpoint is considered to occur when the entropy generation number is minimized, thereby minimizing the overall power required to achieve both desired heat exchange and mass flow rates. Alternatively, irreversible losses of energy availability (or exergy), due to heat exchange and dissipation of kinetic energy to internal energy, are minimized.

4. Results and discussion

In this section, numerical results are presented to demonstrate examples of the micro-profiling technique for reducing surface friction and entropy production. Fig. 3 compares predicted values of entropy generation for parallel embedded microchannels and a benchmark solution for external flow without microchannels (docu-

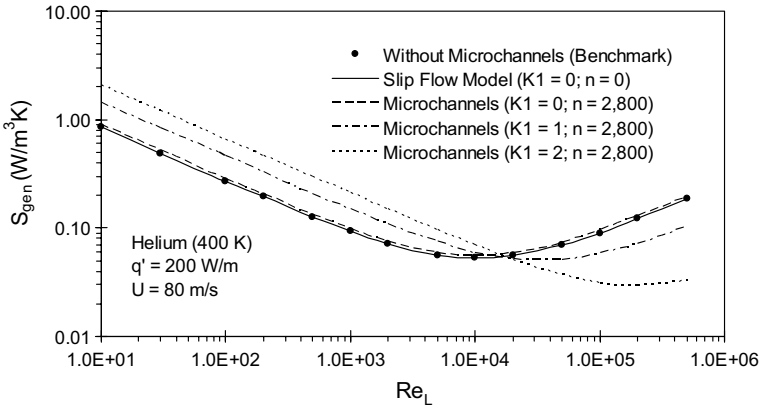

Fig. 3. Comparison of predicted entropy generation with benchmark result.

mented in Ref. [16]). Helium flow at 400 K and a surface heat transfer rate of 200 W/m are considered. Other problem parameters are shown in Fig. 3.

It can be observed that the embedded surface microchannels (dashed lines) have successfully reduced the entropy production below the minimum value obtained without microchannels (benchmark solution). Lower friction irreversibilities due to slip-flow conditions and reduced drag within each microchannel, overcome the added irreversibility of larger surface area with the embedded surface microchannels, particularly as the slip coefficient increases.

In Fig. 3, the predicted results agree closely with the benchmark solution when the slip coefficient becomes zero (i.e., no-slip limit case). Since the microchannels occupy additional surface area with friction, the result with 2800 microchannels and $K_1 = 0$ slightly exceeds the benchmark result. The minimum point is shifted rightwards when the slip coefficient increases. The entropy production continues decreasing at higher Reynolds numbers (or plate lengths). The proportion of friction irreversibility decreases at higher slip coefficients, relative to the thermal irreversibility.

The change of optimal Reynolds number at varying temperatures is depicted in Fig. 4. Air flow at 40 m/s with 1500 embedded parallel microchannels is considered. Other problem parameters are shown in Fig. 4. Heat fluxes of $q' = 10$ W/m (lower set of curves) and $q' = 100$ W/m (upper set of curves) are considered. The results for $Re_{L,\mathrm{opt}}$ are shown, while the optimal plate length can be obtained after multiplying $Re_{L,\mathrm{opt}}$ by kinematic viscosity and dividing by freestream velocity.

The optimal plate length minimizes the exergy destruction of friction and thermal irreversibilities, thereby minimizing the net power required to deliver specified rates of heat exchange and mass flow across

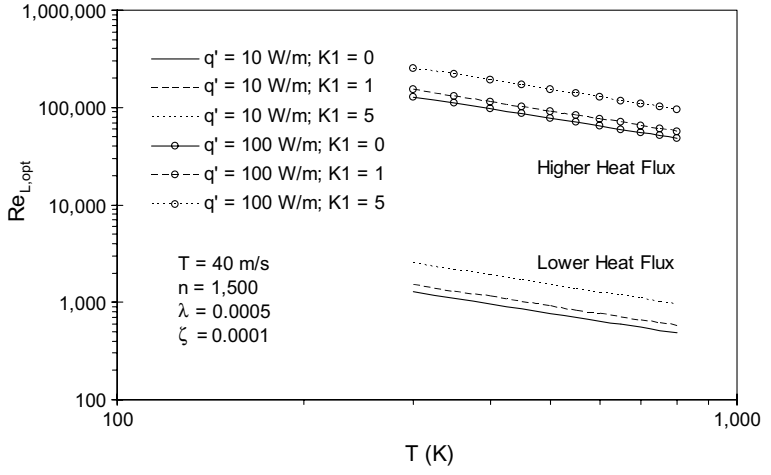

Fig. 4. Change of optimal Reynolds number with temperature.

the surface. For Reynolds numbers below $Re_{L,\mathrm{opt}}$, the friction irreversibility is reduced with a smaller surface area and net friction, but higher thermal irreversibilities arise due to a higher surface temperature and input power needed to transfer q' over a smaller area. On the other hand (values above $Re_{L,\mathrm{opt}}$), the thermal irreversibility decreases with a larger surface area available to transfer the fixed heat flow. But this reduction comes at the expense of higher friction irreversibility, when the larger surface area leads to added surface friction.

Thus, the thermal irreversibility increases and the friction irreversibility diminishes when the surface length becomes smaller, thereby yielding a crossover point at $Re_{L,\mathrm{opt}}$ where entropy production is minimized. The thermal irreversibility is proportional to ΔT (temperature difference between fluid and wall) and q' (heat flow rate), while being inversely proportional to T^2 (freestream temperature). The crossover point at the intersection of each irreversibility curve occurs at $Re_{L,\mathrm{opt}}$, which decreases when the freestream temperature rises (see Fig. 4). Also, Fig. 4 indicates that $Re_{L,\mathrm{opt}}$ decreases with lower slip coefficients, at a given freestream temperature and surface heat flux. The friction irreversibility rises slower and the crossover point of optimality is reduced. The solid line curves with $K_1 = 0$ in Fig. 4 outline the limiting case of no-slip conditions for boundary layer flow.

Air flow at 290 K and 1200 converging surface microchannels with an exit angle of 0.85 rad is studied in Fig. 5. The change of optimal Reynolds number with varying base angle, heat flux and slip coefficient is shown. For each case, $Re_{L,\mathrm{opt}}$ reaches a maximum value at a certain base angle. This angle largely affects the proportion of no-slip conditions over the plate, thereby altering the relative magnitudes of friction and thermal irreversibility. The value of $Re_{L,\mathrm{opt}}$ rises when added surface area is needed to overcome higher thermal irreversibility and minimize the combined friction and thermal irreversibilities.

In Fig. 5, $Re_{L,\mathrm{opt}}$ increases at higher surface heat flows and lower slip coefficients. In the former case, the thermal irreversibility rises at higher wall heat transfer rates, while additional surface area (higher Reynolds number) offsets this trend with added surface friction. Similarly, added plate length and surface friction are considered to offset the reduction of friction irreversibility at lower slip coefficients.

Similar trends with respect to the exit angle are observed in Fig. 6, except that a minimum point of $Re_{L,\mathrm{opt}}$ arises, rather than a maximum point. Air flow at 300 K with a wall heat transfer rate of 20 W/m is investigated. The optimal Reynolds number remains nearly constant with 100 microchannels, as no-slip conditions have a minor impact when the plate is predominantly covered with a flat no-slip surface.

As discussed previously, $Re_{L,\mathrm{opt}}$ increases at lower slip coefficients. The slip coefficient depends on the tangential momentum accommodation coefficient at the wall, which changes with the near-wall effective roughness of the embedded microchannels. An important parameter affecting this coefficient involves the local Knudsen number. In this application, the Knudsen number is determined from the microchannel depth and width. Otherwise, a shallow depth and large width could produce the same Knudsen number, but without realistically yielding slip-flow conditions. Altering the geometrical profile of the embedded microchannel could influence the slip coefficient, based on its dependence on the local Knudsen number.

The Knudsen number, Kn, characterizes the degree of rarefaction of fluid motion. It represents the ratio of the mean free path of molecules to a characteristic length scale of the problem. The continuum assumption of fluid

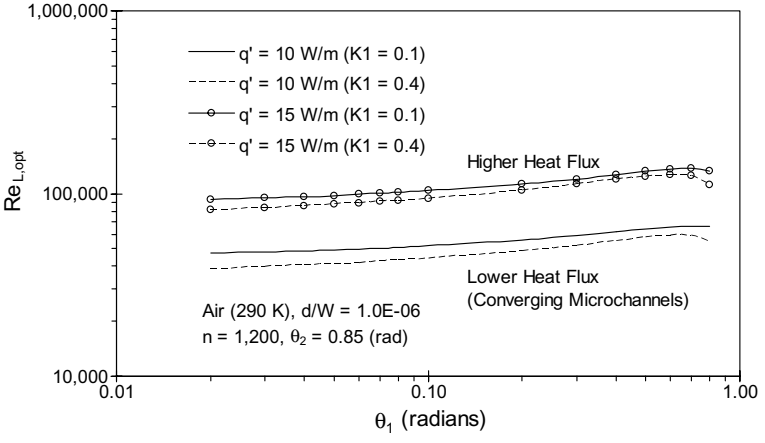

Fig. 5. Change of optimal Reynolds number (converging microchannels).

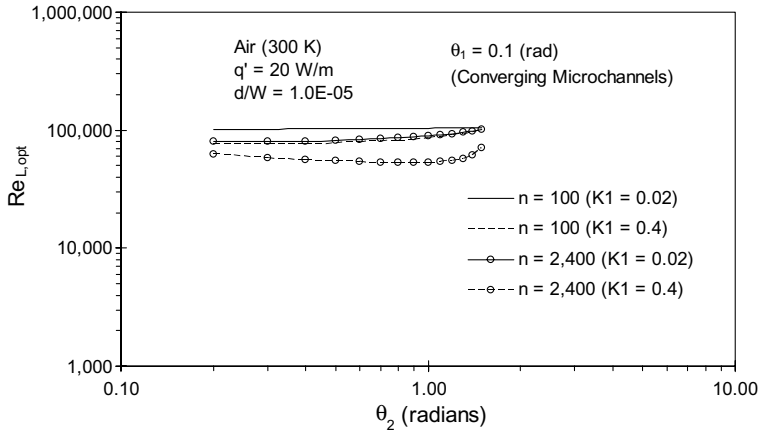

Fig. 6. Change of optimal Reynolds number with varying contraction angle.

flow is considered to be valid when $Kn \leqslant 10^{-3}$, while free molecular flow occurs when $Kn \geqslant 10$. Between these two limits, the slip-flow regime exists within the range of $10^{-3} \leqslant Kn \leqslant 10$ and a transition region occurs for $10^{-3} \leqslant Kn \leqslant 1$. A similar condition of temperature discontinuity exists for the thermal problem, but "no-jump" (thermal problem) replaces the expression of "no-slip" (flow problem). The boundary between the slip-flow and transition regimes is considered to be problem and geometry dependent.

The principles underlying the no-slip/no-jump conditions for velocity and temperature require that there cannot be any finite discontinuities of velocity/temperature at the wall. Such discontinuities would entail infinite velocity and temperature gradients, thereby leading to infinite viscous stresses and heat fluxes. Based on continuum theory, the no-slip/no-jump conditions require an infinitely high number of collisions between the fluid and solid surface. In practice, such assumptions lead to reasonably accurate predictions, provided that $Kn \leqslant 0.001$ for gases.

But for flows at higher Knudsen numbers, the mean free path of molecules is no longer small compared to a characteristic length of the micron or sub-micron device (such as the microchannel height). In the transition to slip-flow conditions, the classical definition of bulk viscosity may become invalid. A molecule may reflect from several walls before colliding with a fluid molecule traveling in the principle flow direction. Additionally, a molecule may travel a distance of several channel heights before colliding with another molecule. Thus, the presence of the wall is less effectively propagated to the fluid molecules traveling in the principle flow direction. These processes have significance when interpreting various trends of varying slip coefficients in previous results.

Another sensitivity study involving $Re_{L,\mathrm{opt}}$ is depicted in Fig. 7. It is known that the friction irreversibility rises and the thermal irreversibility falls with larger

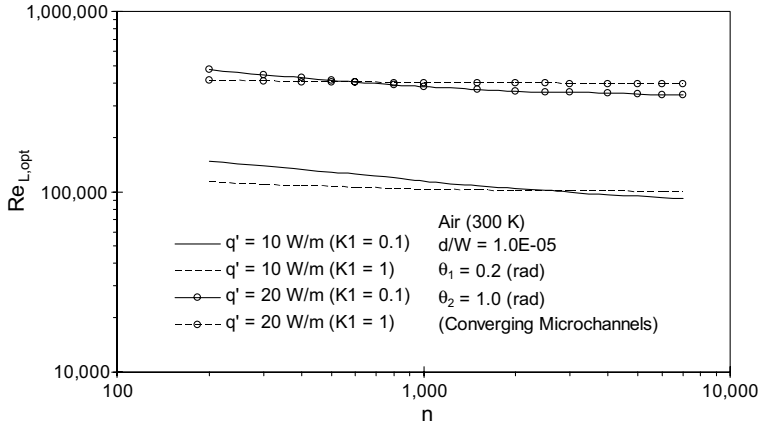

Fig. 7. Change of optimal Reynolds number with varying number of microchannels.

Table 1
Coefficients of entropy generation number

$N_s = \frac{\dot{S}_{gen}}{\dot{S}_{gen,opt}} = a\left(\frac{Re_L}{Re_{L,opt}}\right)^b + c\left(\frac{Re_L}{Re_{L,opt}}\right)^d$	a	b	c	d
Embedded surface microchannels	0.5	−0.5	0.5	0.5
Plate; condensation	0.667	−0.667	0.333	1.333
Tube; internal flow	0.856	−0.8	0.144	4.8
Plate; external flow (laminar boundary layer)	0.5	−0.5	0.5	0.5

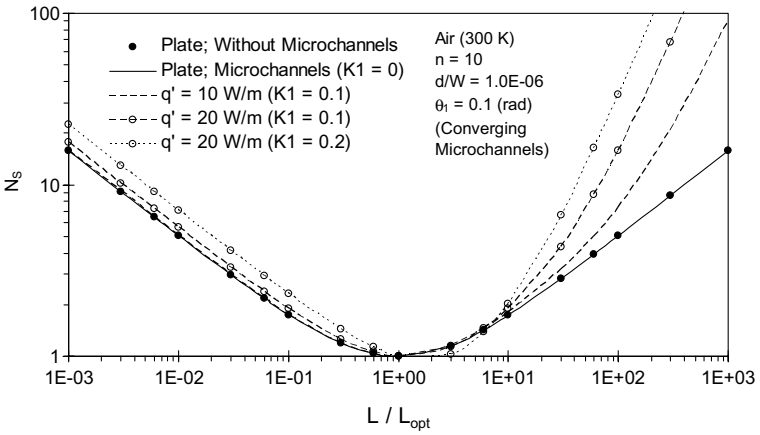

Fig. 8. Comparison of predicted entropy generation number with benchmark result.

surface area. Surface friction increases when the plate length increases, but a smaller temperature difference is needed to transfer a specified heat flow. Fig. 7 suggests that the optimal surface length decreases when more converging surface microchannels are added. Added surface area appears to slightly offset the reduced friction of lower slip coefficients, so a shorter plate length is needed to minimize the combined friction and thermal irreversibilities. It is interesting to observe that a crossover point occurs, with a crossover at fewer microchannels for the higher heat flux case. At the crossover point for a specified heat flux, a smaller optimum crosses over and becomes a relatively longer length, as compared with the lower slip coefficient curve. The thermal irreversibility decreases with additional microchannels, but the change of friction irreversibility to offset that reduction varies with slip coefficient.

Additional comparisons of entropy generation trends are shown in Table 1 for various flow configurations, including forced convection [20], condensation of steam at 1 atm [25] and parallel surface microchannels. The previous studies of film condensation considered both interfacial shear stress and gravitational effects on the film flow along the flat surface [24]. The entropy generation numbers for external flow with embedded microchannels and film condensation are lower than the case involving tube flow. In the latter case, surface curvature of the tube requires that the area available to momentum and heat transfer diminishes in the radial direction, when the fluid is heated by the wall. Thus, higher entropy production arises with larger resulting gradients of temperature and velocity near the wall, since those spatial gradients characterize the thermal and friction irreversibilities therein.

Although Table 1 suggests that the correlation coefficients of entropy production for parallel microchannels matches the case without microchannels, Fig. 8 confirms that the entropy generation numbers can be controlled with micro-profiling of converging surface microchannels. The results demonstrate that drag reduction of slip-flow conditions within embedded surface microchannels can successfully reduce entropy production of convective heat transfer in external flow applications.

5. Conclusions

Surface micro-profiling provides a useful technique of reducing entropy production of convective heat transfer. Reduced drag of slip-flow conditions within the embedded microchannels overcomes the friction irreversibility due to added surface area. A similarity solution of boundary layer flow was used to predict entropy production for both no-slip and slip-flow re-

gimes. The predicted results show that helium flow past 2500 open microchannels and a slip coefficient of 2 yields lower entropy production than standard flat plate flow. The optimal Reynolds number decreases at higher temperatures, higher slip coefficients and more embedded microchannels. Predicted results at the no-slip limit case ($K_1 = 0$) are successfully validated by comparisons to a benchmark result without surface micromachining. Also, comparisons against film condensation and internal tube flow are presented. In contrast to conventional methods of reducing entropy production, such as optimized fins and baffles, the current technique of surface micro-profiling takes advantage of emerging technologies of microfabrication and microfluidic energy conversion.

Acknowledgments

Support of this research from WED (Western Economic Diversification), Westland Helicopters Ltd, CFI (Canada Foundation for Innovation) and NSERC (Natural Sciences and Engineering Research Council of Canada) is gratefully acknowledged. Physical insight regarding slip-flow conditions within the microchannels by Dr. I. Boyd (University of Michigan) and Dr. S. Roy (Kettering University) is appreciated.

References

[1] M. Gad-el-Hak, The fluid mechanics of microdevices—the Freeman scholar lecture, ASME J. Fluids Eng. 121 (1999) 5–33.
[2] G.F. Naterer, S.R. Chomokovski, C. Friesen, C. Shafai, Micro-machined surface channels applied to engine intake flow and heat transfer, AIAA Paper 2003-4054, AIAA 36th Thermophysics Conference, Orlando, FL, June 23–26, 2003.
[3] M.J. Martin, I.D. Boyd, Blasius boundary layer solution with slip flow conditions, in: T.J. Bartel, M.A. Gallis (Eds.), Rarefied Gas Dynamics, Sydney, 2001.
[4] W. Qu, M. Mala, D. Li, Pressure-driven water flows in trapezoidal silicon microchannels, Int. J. Heat Mass Transfer 43 (2000) 353–364.
[5] M. Mala, D. Li, Flow characteristics of water through microtubes, Int. J. Heat Fluid Flow 20 (1999) 142–148.
[6] T.S. Sammarco, M.A. Burns, Heat transfer analysis of microfabricated thermocapillary pumping and reaction devices, J. Micromech. Microeng. 10 (2000) 42–55.
[7] G.M. Wang, E.M. Sevick, M. Mittag, D.J. Searles, D.J. Evans, Experimental demonstration of violations of the second law of thermodynamics small systems and short time scales, Phys. Rev. Lett. 89 (2002) 050601.
[8] S. Tasaki, I. Terasaki, T. Monnai, Comment on experimental demonstration of violations of the second law of thermodynamics for small systems and short time scales, Condensed Matter, arXiv: Physics, Paper 0208154, Cornell University, Ithaca, NY, August 2002.
[9] L. Nummedal, S. Kjelstrup, Equipartition of forces as a lower bound on the entropy production in heat exchange, Int. J. Heat Mass Transfer 44 (15) (2001) 2827–2833.
[10] G.F. Naterer, J.A. Camberos, Entropy and the second law in fluid flow and heat transfer simulation, AIAA J. Thermophys. Heat Transfer 17 (3) (2003) 360–371.
[11] E. Johannessen, L. Nummedal, S. Kjelstrup, Minimizing the entropy production in heat exchange, Int. J. Heat Mass Transfer 45 (13) (2002) 2649–2654.
[12] O.B. Adeyinka, G.F. Naterer, Apparent entropy production difference with heat and fluid flow irreversibilities, Numer. Heat Transfer B 42 (5) (2002) 411–436.
[13] F. Cervantez, J. Solorio, Entropy generation in a plane turbulent oscillating jet, Int. J. Heat Mass Transfer 45 (15) (2002) 3125–3129.
[14] G.F. Naterer, Establishing heat-entropy analogies for interface tracking in phase change heat transfer with fluid flow, Int. J. Heat Mass Transfer 44 (15) (2001) 2903–2916.
[15] G.F. Naterer, Applying heat-entropy analogies with experimental study of interface tracking in phase change heat transfer, Int. J. Heat Mass Transfer 44 (15) (2001) 2917–2932.
[16] G.F. Naterer, Heat Transfer in Single and Multiphase Systems, CRC Press, Boca Raton, FL, 2002.
[17] A. Bejan, A study of entropy generation in fundamental convective heat transfer, ASME J. Heat Transfer 101 (4) (1979) 718–725.
[18] M.L. Merriam, Towards a rigorous approach to artificial dissipation, AIAA Paper 89- 0471, AIAA 27th Aerospace Sciences Meeting and Exhibit, Reno, NV, Jan. 9–12, 1989.
[19] G.F. Naterer, Constructing an entropy-stable upwind scheme for compressible fluid flow computations, AIAA J. 37 (3) (1999) 303–312.
[20] A. Bejan, Entropy Generation through Heat and Fluid Flow, John Wiley and Sons, New York, 1982.
[21] Y. Jaluria, Design and Optimization of Thermal Systems, McGraw-Hill, New York, 1998.
[22] M.C. Sharatchandra, M. Sen, M. Gad-el-Hak, New approach to constrained shape optimization using genetic algorithms, AIAA J. 36 (1) (1998) 51–61.
[23] D. Wang, G.F. Naterer, G. Wang, Thermofluid optimization of a heated helicopter engine cooling bay, Can. Aeronaut. Space J. 49 (2) (2003) 73–86.
[24] C.H. Choi, K.J.A. Westin, K.S. Breuer, To slip or not to slip—water flows in hydrophilic and hydrophobic microchannels, in: Proceedings of IMECE 2002—33707, International Mechanical Engineering Conference and Exposition, New Orleans, LA, Nov. 13–16, 2002.
[25] O.B. Adeyinka, G.F. Naterer, Optimization correlation for entropy production and energy availability in film condensation, Int. Commun. Heat Mass Transfer 31 (4) (2004) 513–524.